ADVANCED ELECTRONIC MATERIALS
Open Access
www.advelectronicmat.de

Check for updates

Ultrahigh Performance UV Photodetector by Inserting an Al_2O_3 Nanolayer in NiO/n-Si

Xingzhao Ma, Libin Tang, Menghan Jia, Yuping Zhang, Wenbin Zuo, Yuhua Cai, Rui Li, Liqing Yang, and Kar Seng Teng**

Ultraviolet (UV) photodetectors have gained much attention due to their numerous important applications ranging from environmental monitoring to space communication. To date, most p-NiO/n-Si heterojunction photodetectors (HPDs) exhibit poor UV responsivity and slow response. This is mainly due to a small valence band offset (ΔE_V) at the NiO/Si interface and a high density of dangling bonds at the silicon surface. Herein, an UV HPD consisting of NiO/Al_2O_3/n-Si is fabricated using magnetron sputtering technique. The HPD has a large rectification ratio of 2.4×10^5. It also exhibits excellent UV responsivity (*R*) of 15.8 A/W at −5 V and and detectivity (*D) of 1.14×10^{13} Jones at −4 V, respectively. The excellent performance of the HPD can be attributed to the defect passivation at the interfaces of the heterojunction and the efficient separation of photogenerated carriers by the Al_2O_3 nanolayer. The external quantum efficiency (*EQE*) of the HPD as high as 5.4×10^3%, hence implying a large optical gain due to carrier proliferation resulting from impact ionization. Furthermore, the ultrafast response speed with a rise time of 80 μs and a decay time of 184 μs are obtained.**

1. Introduction

UV photodetector has been widely used in ozone monitoring, flame sensing, optical communication and space research.[1–4] One of the commonly used semiconductor materials in photodetectors is silicon due to its integrability, compatibility with CMOS process, well-established manufacturing process and high-speed detection capability.[5] However, silicon-based photodetectors encounter several issues in the UV region, such as low photoresponse due to high reflection coefficient and shallow UV penetration depth. NiO, a wide bandgap (3.4–4.1 eV) semiconductor that strongly absorbs UV light, is a good alternative material for UV photodetector.[6] Due to the existence of non-stoichiometric Ni vacancies and interstitial oxygen, NiO exhibits intrinsic p-type conduction and high hole mobility. Therefore, NiO is often used as p-type semiconductor in conjunction with n-Si in the construction of silicon-based PN junction UV photodetectors exhibiting high charge separation and collection efficiency. For instance, NiO nanowire/n-Si HPD was developed and demonstrated responsivity and detectivity of 9.1 mA/W and 1.8×10^9 Jones, respectively, under 365 nm at 0 V.[6] Also, silicon-based UV photodetector consisting of p-NiO film demonstrated good photovoltaic characteristics with responsivity of 0.15 A/W under 290 nm at 0 V.[7] However, the dangling bonds at silicon surface of NiO/n-Si UV HPDs act as recombination centers, hence leading to a large dark current.[8] Moreover, due to the small ΔE_V of the NiO/n-Si interface, the photogenerated holes in the silicon can be easily extracted into the external circuit, thereby reducing the light-dark current ratio and UV–vis ratio.[9,10]

An ultra-thin layer of dielectric materials, such as SiO_2,[11,12] Al_2O_3,[13–15] and MgO,[16] have previously been used to passivate dangling bonds at the surface of silicon and defect states at the heterojunction interface. Among these dielectric layers, Al_2O_3 has been effective as a carrier blocking layer to improve the efficiency of carrier separation as well as a buffer layer to enhance the crystal quality of films.[13] Furthermore, Al_2O_3 also acts a tunneling layer and has passivation effect at the heterojunction that will improve the thermodynamic stability at the interfacial contact.[17] T. Wang et al. fabricated a ZnO/Al_2O_3/p-Si HPD and reported an increase of photoluminescent (PL) intensity at the

X. Ma, L. Tang
School of Materials and Energy
Yunnan University
Kunming 650500, China
E-mail: scitang@163.com

X. Ma, L. Tang, M. Jia, Y. Zhang, W. Zuo, Y. Cai, R. Li, L. Yang
Kunming Institute of Physics
Kunming 650223, China

X. Ma, L. Tang, M. Jia, Y. Zhang, W. Zuo, Y. Cai, R. Li, L. Yang
Yunnan Key Laboratory of Advanced Photoelectric Materials & Devices
Kunming 650223, China

M. Jia
School of Physics and Astronomy
Yunnan University
Kunming 650500, China

K. S. Teng
Department of Electronic and Electrical Engineering
Swansea University
Bay Campus, Fabian Way, Swansea SA1 8EN, UK
E-mail: k.s.teng@swansea.ac.uk

The ORCID identification number(s) for the author(s) of this article can be found under https://doi.org/10.1002/aelm.202300909

© 2024 The Author(s). Advanced Electronic Materials published by Wiley-VCH GmbH. This is an open access article under the terms of the Creative Commons Attribution License, which permits use, distribution and reproduction in any medium, provided the original work is properly cited.

DOI: 10.1002/aelm.202300909

device by 58%, while the dark current decreased by an order of magnitude with the addition of Al_2O_3 dielectric layer.[13] H. Qian et al. compared the photoelectric performances of Ga_2O_3/p-Si and Ga_2O_3/Al_2O_3/p-Si HPDs. The dark current of the latter was reduced by four orders of magnitude, and its detectivity improved by two orders of magnitude under 254 nm UV light. Meanwhile, the response and recovery speed of the device were reduced by 3.7 and 8.2 times, respectively.[15] It follows that the insertion of Al_2O_3 layer between silicon and metal oxide can effectively improve the photoelectric characteristics of HPD and therefore enhancing the device performances. However, most Al_2O_3 layers are prepared using complex and expensive techniques, such as atomic layer deposition (ALD) and metal-organic chemical vapor deposition (MOCVD), and achieving uniformity on large area film remains a challenge.

Herein, a NiO/Al_2O_3/n-Si UV HPD was fabricated using a facile and low-cost magnetron sputtering technique. The HPD exhibited a low dark current of 279 nA at −5 V and a high rectification ratio of 2.4×10^5 at ±5 V. The device also demonstrated excellent R, D^* and EQE of 15.8 A/W, 1.03×10^{13} Jones and 5.4×10^3%, respectively, under 365 nm illumination at −5 V. It has a fast response speed with rise and decay times of 80 and 184 μs at −3 V, respectively.

2. Experimental Section

NiO, Al_2O_3, and Au sputtering targets (99.99%) were purchased from Zhongnuo Advanced Material (Beijing) Technology Co. Ltd. A n-Si (1 0 0) wafer (resistivity of 1–3 Ω·cm) with thickness of 400±25 μm was purchased from Suzhou Research Material Micro-nano Technology Co. Ltd. All chemical reagents were used without further purification.

NiO/Al_2O_3/n-Si heterojunction was fabricated by depositing Al_2O_3 and NiO films on n-Si substrate using magnetron sputtering technique at room temperature. **Figure 1a** shows schematic diagrams on the preparation process of the heterojunction. Prior to sputtering, the Si wafer was ultrasonically cleaned with acetone, ethanol and deionized water in turn for 10 min at each step. The Si wafer was then dipped into buffered oxide etchant (HF:H_2O = 1:50) for 20 s to remove native oxide. Finally, the Si wafer was rinsed with deionized water and blown dried using nitrogen. The sputtering parameters, such as pressure, power, time and argon flow rate, for Al_2O_3 film were 5 Pa, 100 W, 50 s and 50 sccm, and for NiO film were 0.43 Pa, 200 W, 50 min and 50 sccm, respectively. In order to minimize lattice damage caused by magnetron sputtering and enhance the crystallinity of the films, the deposited films were annealed in the air atmosphere at 300 °C for 1 h.

The crystal structure of NiO thin film was studied using transmission electron microscopy (TEM, Tecnai G2 TF30) and X-ray diffraction (XRD, Rigaku D/Max-23). Element analysis of the NiO film was performed by X-ray photoelectron spectroscopy (XPS, K, Alpha+). The field emission scanning electron microscopy (SEM, NOVA NANOSEM 450) was used to characterize the surface morphology of NiO and Al_2O_3 films. Cross-sectional SEM image of NiO/Al_2O_3/n-Si heterojunction was obtained to allow thickness measurements of each film layer. The thickness of Al_2O_3 ultrathin layer was measured using atomic force microscopy (AFM, Bruker Dimension ICON). The absorption spectra of NiO film on quartz substrate were acquired using UV–vis absorption spectrometer (UV-3600PLUS), which provides a basis for the estimation of the optical bandgap of NiO film. All characterizations, except XRD, were performed on annealed films.

Figure 1b depicts the fabrication process of the NiO/Al_2O_3/n-Si UV HPD (denoted as HPD-B) by magnetron sputtering technique. Au films/electrodes with a thickness of 100 nm were deposited onto the NiO/Al_2O_3/n-Si heterojunction to collect electrons and holes. For the anode, the NiO side was masked before sputtering and the mask was then removed after sputtering, hence leaving an exposed area of 0.04 cm^2 as photosensitive region at the NiO film. Similarly, Au film was deposited on the n-Si side as the cathode. Finally, Au wires were connected to the Au electrodes using silver paste. A NiO/n-Si UV HPD (denoted as HPD-A) was fabricated using similar method for comparative study. A Keithley 2400 sourcemeter and an Agilent oscilloscope (DSO-X 4054A) were used to characterize the electrical properties of two type HPDs. All measurements were carried out at room temperature under ambient conditions.

3. Results and Discussion

TEM and XRD characterizations were performed to study the crystal structures of NiO and Al_2O_3 films.**Figure 2a,b** shows the TEM and HRTEM images of NiO film, respectively. The lattice fringe spacings of 0.209, 0.147, and 0.241 nm correspond to the (0 1 2), (1 1 0), and (1 0 1) crystal faces of NiO, respectively. The corresponding atomic spatial arrangements of the different crystal planes of NiO are shown in Figure 2c–e.

Figure 3a,b shows the XRD patterns of NiO and Al_2O_3 films deposited on Si substrate, respectively. The two characteristic peaks corresponding to (1 0 1) and (1 1 0) crystal planes are evident in the XRD pattern of the unannealed (UA) NiO film. A narrow full width half maximum (FWHM) of these peaks suggest that the NiO film is of good crystallinity before annealing. The diffraction intensity of these peaks associated with annealed (A) NiO film has slightly increased, while its FWHM remains unchanged. However, there is an increase in the number of characteristic peaks in the XRD pattern of annealed NiO film. It reveals three characteristic peaks corresponding to the (1 0 1), (0 1 2), and (1 1 0) crystal planes of NiO, which belong to the hexagonal R-3m space group, after annealing. This is consistent with the PDF standard card (JCPDS PDF#44-1159), and in agreement with the TEM characterization of NiO film. For unannealed (UA) Al_2O_3 film, the XRD pattern reveals amorphous peaks at 2θ values of 76.442° and 50.673°, which indicate poor crystallinity of the film. The diffraction intensity of the two peaks are enhanced upon annealing (A) of the Al_2O_3 film. Furthermore, its FWHM is also reduced. A characteristic peak that corresponds to the (2 0 5) crystal face can be observed at 2θ value of 64.576°, which conforms to JCPDS PDF#26-0031, hence indicating that the crystallinity of the Al_2O_3 film is enhanced by the annealing treatment.

The chemical bond of NiO was characterized using XPS. Figure 3c,d shows the XPS spectra of Ni and O elements, respectively. The Ni 2p core level consists of doublet peaks (i.e., Ni $2p_{3/2}$ and Ni $2p_{1/2}$) as shown in Figure 3c. The Ni $2p_{3/2}$ peak are deconvoluted into three peaks located at 854.69, 856.16, and 861.48 eV. The peak at 854.69 eV is associated with the presence of NiO.[9] While the peaks at 856.16 and 861.48 eV are the main and

© 2024 The Author(s). Advanced Electronic Materials published by Wiley-VCH GmbH
2199160x, 2024, 9, Downloaded from https://onlinelibrary.wiley.com/doi/10.1002/aelm.202300909 by Test, Wiley Online Library on [27/11/2024]. See the Terms and Conditions (https://onlinelibrary.wiley.com/terms-and-conditions) on Wiley Online Library for rules of use; OA articles are governed by the applicable Creative Commons License

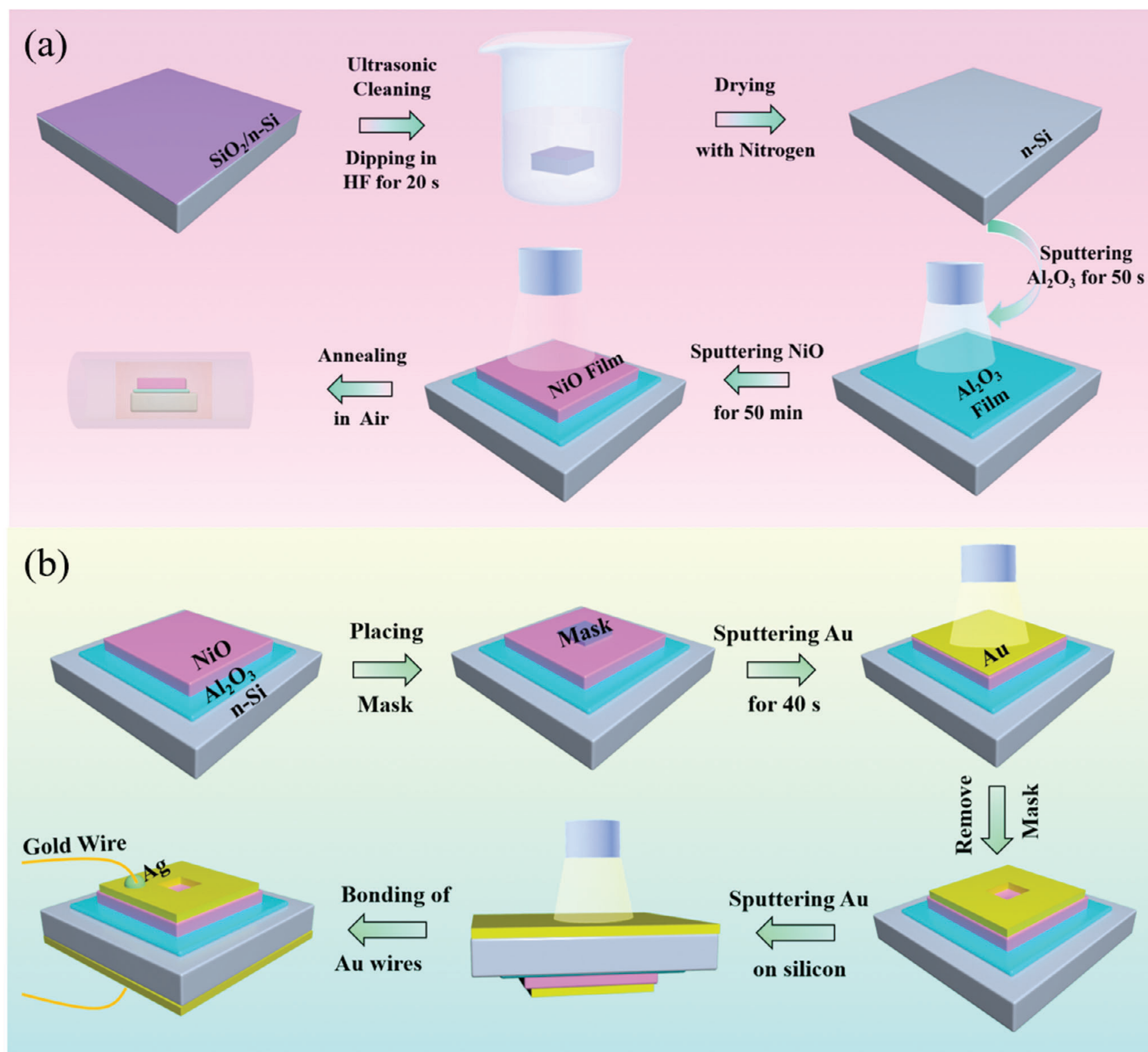

Figure 1. Schematic diagrams illustrating the fabrication process of a) NiO/Al_2O_3/n-Si heterojunction and b) NiO/Al_2O_3/n-Si HPD.

satellite peaks of Ni $2p_{3/2}$, respectively, indicating the existence of Ni^{2+} (i.e., NiO) due to the interaction of Ni–O.[18] The other two deconvoluted peaks, located at 873.52 (main peak) and 879.68 eV (satellite peak), are associated with NiO of Ni $2p_{1/2}$ in stoichiometric NiO.[19] The XPS spectrum of O 1s is shown in Figure 3d. The O 1s core level peak is deconvoluted into two components related to oxygen vacancy (O_V) and lattice oxygen (O_L) at 531.68 and 530.21 eV, respectively. These two peaks are attributed to Ni—O.[18]

FESEM images revealing the surface morphology of NiO and Al_2O_3 films are shown in Figure 3e,f, respectively. Prismatic particles with clear boundaries can be observed at the NiO film. The size of these particles is relatively uniform with an average size of ≈100 nm. As for Al_2O_3 film, it contains fine and dense particles that are uniformly distributed across the surface. Cross-sectional SEM image of the NiO/Al_2O_3/n-Si heterojunction is shown in Figure 3g.

It is found that the NiO film has a longitudinal dense growth pattern. The thickness of each deposited layer has a crucial effect on the performance of the device. From the image, the thickness of NiO and Al_2O_3 films can be estimated as 618.2 and 5.0 nm, respectively. Figure 3h shows the AFM topography of the Al_2O_3 film. The line profile (inset) shows the Al_2O_3 film having a thickness of 5.0 nm, which is consistent with the thickness estimated from the SEM image in Figure 3g.

The UV–vis absorption spectrum of NiO film is shown in Figure 3i. The absorption of NiO film is strongest at the wavelength range of 260–300 nm, and gradually weakens beyond 300 nm. There is almost no absorption in visible region.

© 2024 The Author(s). Advanced Electronic Materials published by Wiley-VCH GmbH

2199160x, 2024, 9, Downloaded from https://onlinelibrary.wiley.com/doi/10.1002/aelm.202300909 by Test, Wiley Online Library on [27/11/2024]. See the Terms and Conditions (https://onlinelibrary.wiley.com/terms-and-conditions) on Wiley Online Library for rules of use; OA articles are governed by the applicable Creative Commons License

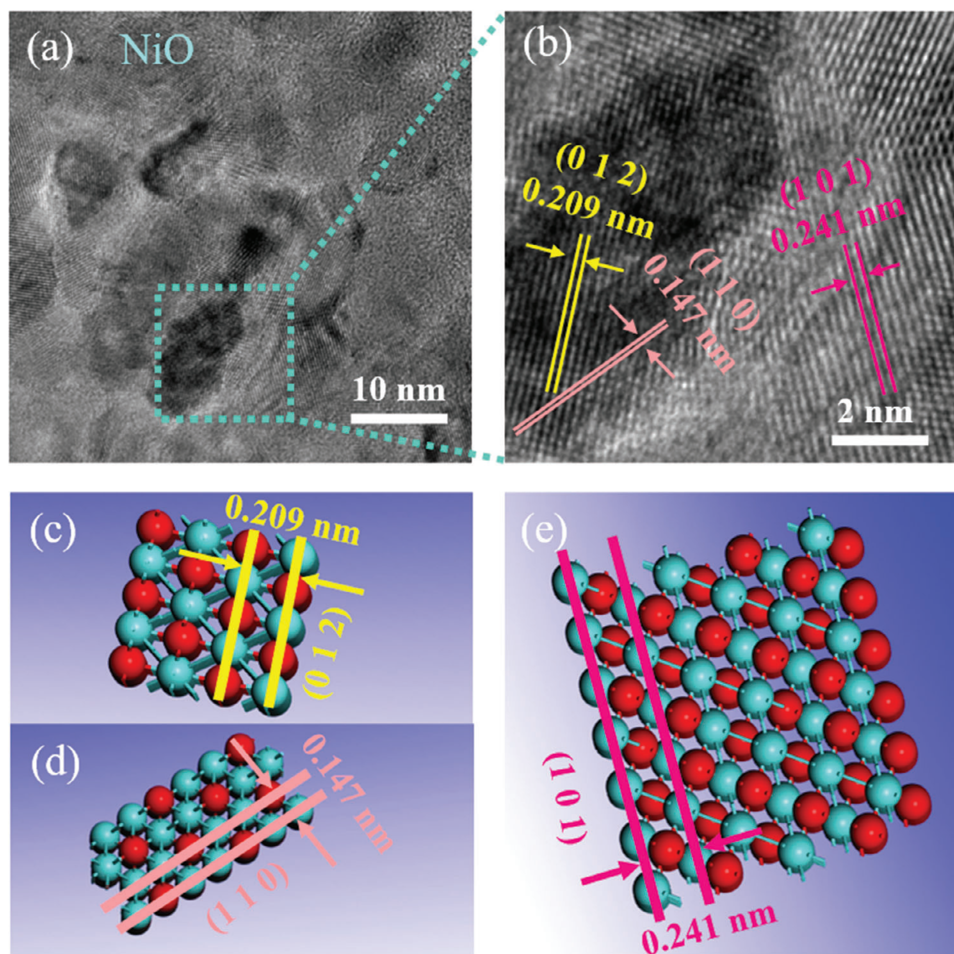

Figure 2. a,b) TEM and HRTEM images of NiO, respectively. c–e) Atomic spatial arrangements of the NiO crystal planes.

Equation 1 can be used to estimate the optical bandgap energy (E_g) of the NiO film:

$$\alpha\ (h\nu) = A\left(h\nu - E_g\right)^{1/2} \tag{1}$$

where α is absorption coefficient, $h\nu$ is photon energy, and A is a constant. A plot of $(\alpha h\nu)^2$cm^{-2} as a function of $h\nu$ is shown in the inset of Figure 3i. Taking into account of the film thickness measured by AFM, the E_g of NiO film is determined to be 3.62 eV, which is within the theoretical E_g range of NiO (3.4–4.1 eV).

I–V characteristics of HPD-A and HPD-B before and after annealing under dark condition are shown in **Figure 4**a. Figure 4b shows the corresponding log *I–V* plots. HPD-A exhibits poor rectification characteristic before annealing and a large leakage current of more than 10^4 µA. After annealing, its rectification characteristic is enhanced and the dark current is reduced to 15 µA. As for unannealed HPD-B, it exhibits some rectification characteristic but has a large dark current of 79 µA. Upon annealing, the HPD-B exhibits significantly improved rectification characteristic, and its dark current is reduced to 94 nA. It is obvious that both annealing treatment and insertion of Al_2O_3 nanolayer could reduce the dark current and increase the rectification ratio of the HPD. For NiO film, the recrystallization process occurs in the film during annealing, which leads to the disappearance of almost all the defects from the sputtering process and greatly reduces the probability of carrier recombination. Furthermore, the crystallinity of the film is further enhanced after annealing, which provides an improved transport path for carriers. As for Al_2O_3 film, the annealing treatment can provide the sputtered particles with dynamic energy, which promotes the migration of the particles to suitable lattice sites for nucleation and results in film crystallization. The rearrangement of atoms during the annealing treatment would reduce the defect sites at the crystal lattice of Al_2O_3, which results in good quality NiO/Al_2O_3 and Al_2O_3/Si interfaces, hence improving the carrier transmission efficiency. Therefore, this has led to a decrease in the leakage current in both HPD-A and HPD-B after annealing. The performance improvement is also attributed to the passivation effects of Al_2O_3 layer on the dangling bonds at the silicon surface and the defect states at the heterojunction interface as well as the large ΔE_V (4.03 eV) of the Al_2O_3/n-Si heterojunction that prevents holes in the silicon from being extracted into the external circuit. To investigate the photoelectric response characteristics of HPDs, a LED light with wavelength of 365 nm and optical power density of 5.8 mW cm^{-2}

© 2024 The Author(s). Advanced Electronic Materials published by Wiley-VCH GmbH

2199160x, 2024, 9, Downloaded from https://onlinelibrary.wiley.com/doi/10.1002/aelm.202300909 by Test, Wiley Online Library on [27/11/2024]. See the Terms and Conditions (https://onlinelibrary.wiley.com/terms-and-conditions) on Wiley Online Library for rules of use; OA articles are governed by the applicable Creative Commons License

2199160x, 2024, 9, Downloaded from https://onlinelibrary.wiley.com/doi/10.1002/aelm.202300909 by Test, Wiley Online Library on [27/11/2024]. See the Terms and Conditions (https://onlinelibrary.wiley.com/terms-and-conditions) on Wiley Online Library for rules of use; OA articles are governed by the applicable Creative Commons License

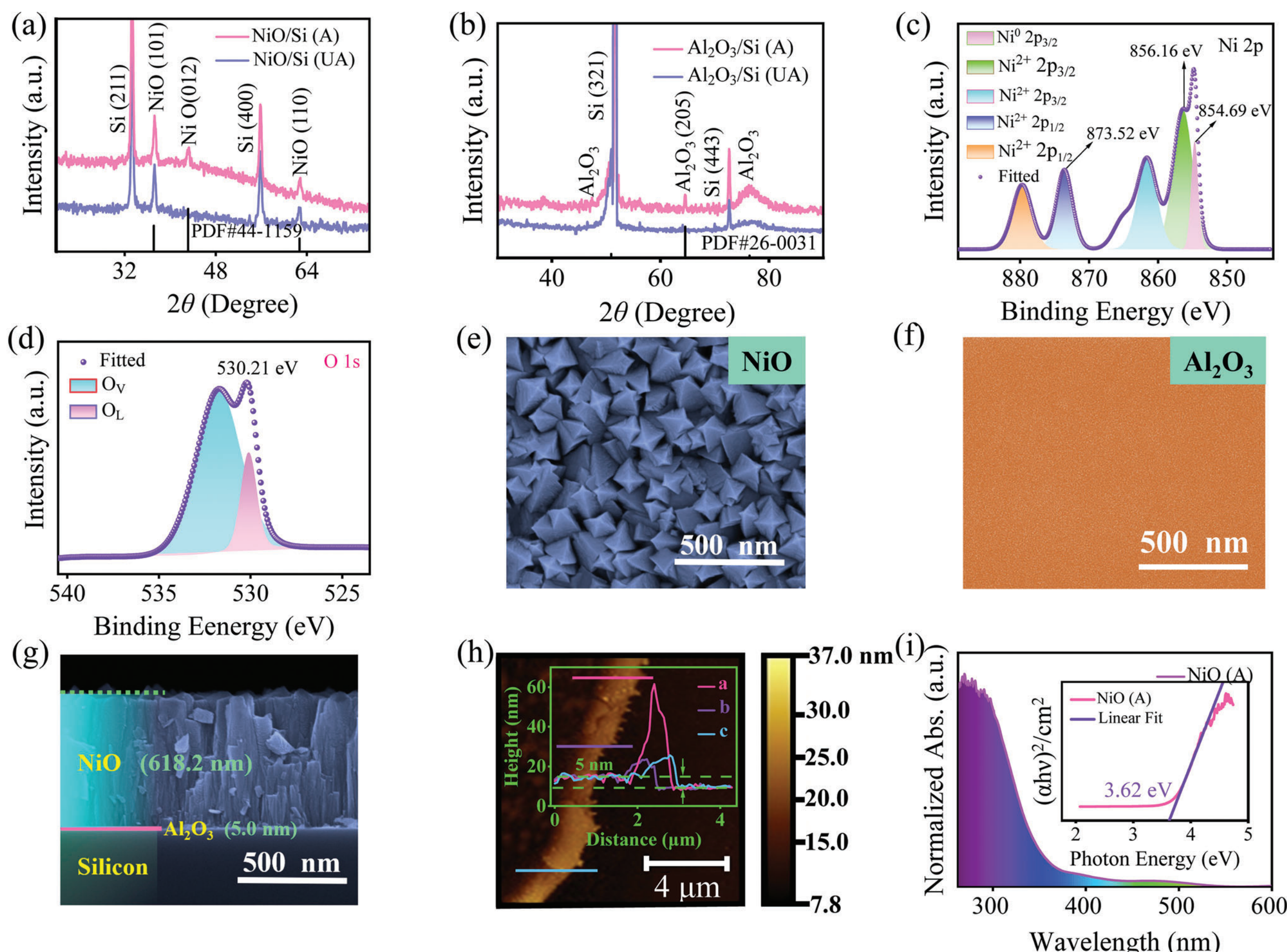

Figure 3. a,b) XRD patterns of NiO and Al_2O_3 films, respectively. c,d) XPS spectra of Ni 2p and O 1s core levels at NiO film, respectively. e,f) SEM images of NiO and Al_2O_3 films, respectively. g) Cross-sectional SEM image of NiO/Al_2O_3/n-Si heterojunction. h) AFM image and line profiles (inset) for thickness measurement of Al_2O_3 film. i) UV–vis absorption spectrum of the NiO film and the inset shows the plots of $[\alpha(h\nu)]^2$ versus photon energy.

was irradiated on to the photosensitive regions of both annealed HPD-A and HPD-B. It is worth noting that the LED illuminated area is much larger than the photosensitive area (red dotted line) as shown in the inset of Figure 4c–e. Figure 4c,d shows the *I–V* and log *I–V* plots of HPD-A, respectively, under illumination and dark conditions.

The inset of Figure 4c depicts the vertical structure of HPD-A consisting of Au/NiO/n-Si/Au. As shown in Figure 4c, the HPD-A exhibits a large dark current of 20 μA at -5 V and a obvious rectification behavior with rectification ratio of 1.1×10^4 within ±5 V, which is due to the existence of built-in electric field at the interface between p-NiO and n-Si. It can be seen from Figure 4d that the light-to-dark current ratio of HPD-A is less than one order of magnitude. This is mainly caused by the defect states and dangling bonds at the NiO/n-Si interface and the small ΔE_V (0.03 eV).[8–10] The *I–V* and log *I–V* plots of HPD-B under light and dark conditions are shown in Figure 4e,f, respectively. The inset of Figure 4e illustrates the vertical structure of HPD-B consisting of Au/NiO/Al_2O_3/n-Si/Au. A low dark current of 279 nA was obtained by HPD-B under a large bias voltage of −5 V. The rectification ratio is 2.4×10^5 within ±5 V, and the light-to-dark current ratio is up to 1.3×10^4. The improvement of the photoresponse performance is mainly attributed to the passivation of the defects at the heterojunction interface of the Al_2O_3 tunneling layer. Al_2O_3 also provides fixed negative charges, which are conducive to hole extraction.[20]

The photoelectric performances of HPD-B are evaluated using key parameters, such as *R*, *D** and *EQE*, which are determined using the following formulas:[21–23]

$$R = \frac{I_{ph} - I_d}{PA} \tag{2}$$

$$D^* = \frac{R}{\sqrt{2eI_d/A}} \tag{3}$$

$$EQE = R\frac{hc}{e\lambda} \tag{4}$$

where I_{ph} and I_d represent photocurrent and dark current, respectively, *P* is power density of incident light, *A* is effective irradiation area, *e* is electron charge, *h* is Planck's constant, *c* is speed of light,

© 2024 The Author(s). Advanced Electronic Materials published by Wiley-VCH GmbH

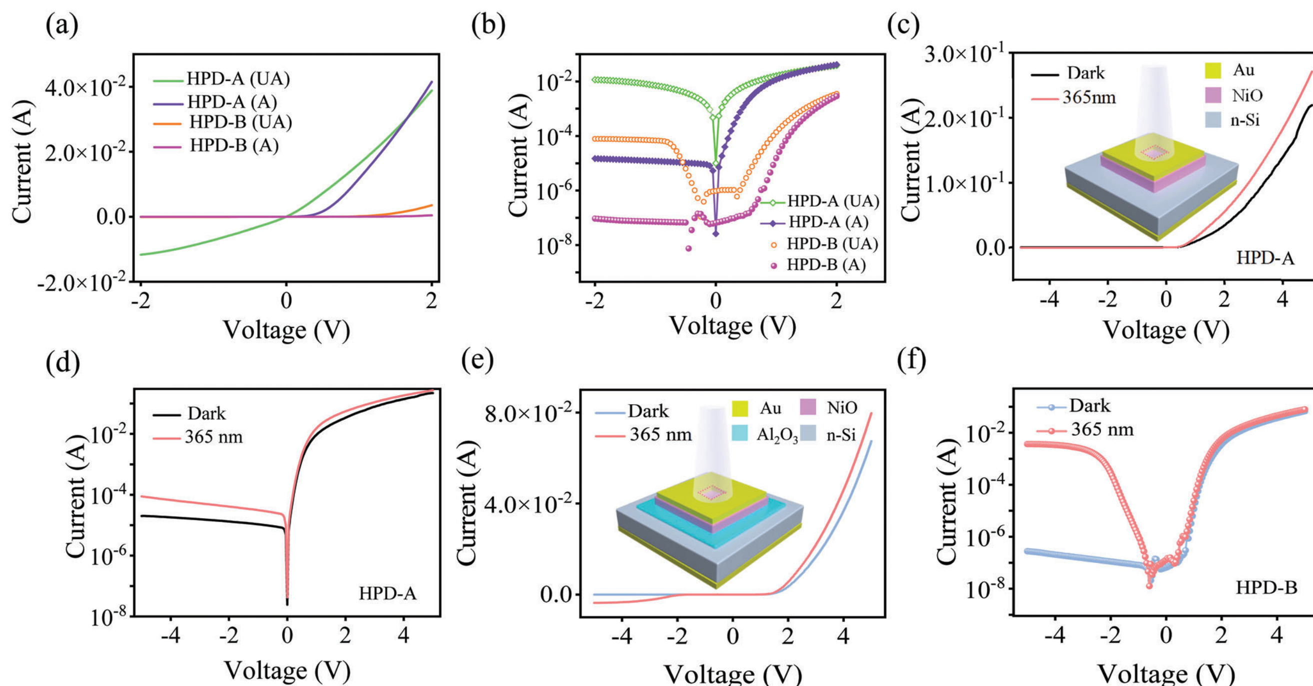

Figure 4. a,b) *I–V* and log *I–V* plots of HPD-A and HPD-B, respectively, under dark condition. c,d) *I–V* and log *I–V* plots of HPD-A under 365 nm illumination and dark conditions, respectively. e,f) *I–V* and log *I–V* plots of HPD-B under 365 nm illumination and dark conditions, respectively.

and λ is wavelength of the incident light. The plots of R and D^* against bias for HPD-B is shown in **Figure 5a**. When the HPD is under low negative bias (<1.7 V), both R and D^* values are relatively low. The values of R and D^* increase significantly with an increase of bias. The maximum values of R and D^* are 15.8 A/W at −5 V and 1.14×10^{13} Jones at −4 V, respectively. Figure 5b shows the EQE plot of HPD-B and the inset shows an enlarged EQE plot from 0 to −1.5 V. The value of EQE remains relatively constant at low negative bias (<1.7 V) but increases rapidly at large negative bias voltage. The value of EQE can be obtained as 5.4×10^3%, which indicates high gain of the HPD-B.

Transient response of HPD-B was characterized under frequency-modulated illumination using a signal generator, a digital oscilloscope and a signal amplifier. As shown in Figure 5c, the HPD exhibits excellent stability and repeatability under 365 nm illumination at 600 Hz modulated frequency with −3 V bias voltage. Rise time is defined as the time it takes for the photocurrent to rise from 10% to 90% of its maximum value, while decay time is the opposite. For a photodetector with photoconductive gain, it usually takes a long time to accumulate photocurrent, resulting in a long response time. However, as shown in Figure 5di,ii, the HPD-B exhibits fast transient response with rise and decay times of 80 and 184 µs, respectively. **Table 1** compares the performances of HPD-B reported in this work with other metal-oxide-based UV HPDs.

Energy band diagrams of HPD-B are illustrated in Figure 5e,f to explain the carrier transport and origin of gain at the device. The electron affinities of n-Si, Al_2O_3 ,and NiO are 4.05, 2.4, and 1.5 eV, and their energy gaps are 1.12, 5.75, and 3.62 eV, respectively.[15] Therefore, the conduction band offset (ΔE_C) at the NiO/Al_2O_3 interface is calculated as 0.9 eV, and the valence band offset (ΔE_V) at the Al_2O_3/n-Si interface is 2.98 eV. The work function of Au is 5.1 eV. Under UV irradiation, photogenerated electron-hole pairs are generated in both NiO and n-Si. At a low bias, the electrons in NiO drift through the ultrathin Al_2O_3, which has higher electron affinity, to reach n-Si and the process is driven by built-in electric field as illustrated in Figure 5e. These electrons, along with the electrons in n-Si, are collected by the cathode. The photogenerated holes in NiO are collected by the anode due to the built-in electric field. However, it is difficult for the photogenerated holes in n-Si to tunnel through the Al_2O_3 layer to reach NiO because of the large ΔE_V (2.98 eV) at the Al_2O_3/n-Si interface. The applied electric field from a small bias voltage is insufficient for a significant number of photogenerated holes to tunnel through the Al_2O_3 layer, hence resulting in an accumulation of photogenerated holes near the Al_2O_3/n-Si interface. As shown in Figure 4f, the photoresponse of HPD-B at small reverse bias voltage (<−1.7 V) is limited. With the increase of reverse bias, the depletion region of the heterojunction become widen and the electric field across the region is enhanced due to the reverse bias produces an electric field in the depletion region in the same direction as the built-in electric field. At −5 V bias, there is a significant acceleration of the photogenerated holes as shown in Figure 5f. The photogenerated holes, which are previously accumulated near the Al_2O_3/n-Si interface, can tunnel through the ultrathin Al_2O_3 and are collected by the anode together with the photogenerated holes in NiO. Furthermore, the accelerating photogenerated holes can potentially impact the crystal lattice of the Al_2O_3 layer and lead to the release of their kinetic energy thereby generating additional carriers within the Al_2O_3 layer. Consequently, an increased number of carriers are generated and collected when the biased voltage is at -5 V. This explains the significant enhancement in the photoresponse of HPD-B as observed in Figure 4f. Also, the proliferation of these carriers

 © 2024 The Author(s). Advanced Electronic Materials published by Wiley-VCH GmbH

2199160x, 2024, 9, Downloaded from https://onlinelibrary.wiley.com/doi/10.1002/aelm.202300909 by Test, Wiley Online Library on [27/11/2024]. See the Terms and Conditions (https://onlinelibrary.wiley.com/terms-and-conditions) on Wiley Online Library for rules of use; OA articles are governed by the applicable Creative Commons License

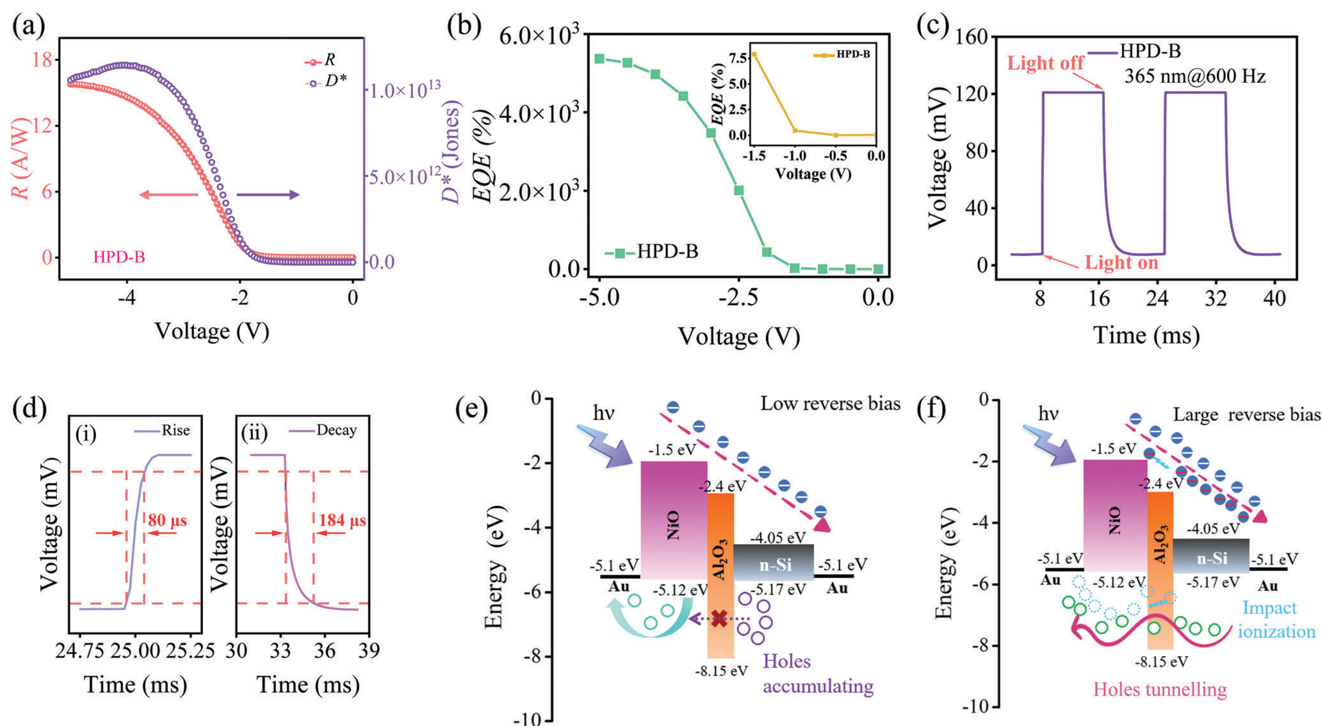

Figure 5. a) R and D^* plots of HPD-B. b) EQE plot of HPD-B and the inset shows the enlarged EQE from 0 to −1.5 V. c) Switching behavior of HPD-B under 365 nm illumination at 0 V. d) Enlarged views of i) rise and ii) decay edges corresponding to (c). e,f) Energy band diagrams of HPD-B at 0 V and −3 V, respectively.

due to impact ionization can result in optical gain achieved by HPD-B.[32,33]

4. Conclusion

In summary, a high performance NiO/Al_2O_3/n-Si UV HPD, consisting of an ultrathin Al_2O_3 nanolayer (≈5.0 nm) between p-NiO and n-Si was fabricated and studied. The device exhibits a low dark current of 279 nA and large rectification ratio of 2.4×10^5. The high D^* of 1.14×10^{13} Jones was obtained at – 4 V. It demonstrates excellent R and EQE of 15.8 A/W and 5.4×10^3% at −5 V, respectively. The high EQE indicates optical gain, which is attributed to the proliferation of carriers resulted from impact ionization at the Al_2O_3 layer. The HPD also exhibits fast response with rise and decay time of 80 and 184 µs, respectively. The Al_2O_3 dielectric layer has the following beneficial effects that enhance the photoresponse of the HPD: i) It passivates the dangling bonds at the silicon surface and defect states at the NiO/n-Si interface to reduce the recombination of carriers. ii) The large ΔE_V at the Al_2O_3/n-Si interface suppresses the dark current in the HPD. (iii) The surface of Al_2O_3 introduces negative fixed charges, which are conducive to the extraction of holes.

Table 1. Comparison of characteristic parameters of UV HPDs based on metal oxide heterostructures.

HPD	Wavelength [nm]	Bias [V]	R [A W^{-1}]	EQE [%]	D^* [Jones]	Rise/decay time [ms]	Ref.
SnO_2/SiO_2/p-Si	365	−1	0.355	–	2.66×10^{12}	<100	[12]
Ga_2O_3/Al_2O_3/p-Si	254	−10	8.1	–	4.21×10^{13}	870/290	[15]
NiO/ZnO/n-Si	280	−1	3.67	–	4.21×10^{12}	10 500/400	[24]
MgZnO/MgO/p-Si	240	6	1.16	600	–	0.015	[25]
NiO/SiO_2/n-ZnO	365	2	5.77	1.96×10^3	1.51×10^{11}	48	[26]
NiO/TiO_2/ZnO	365	2	291	–	6.9×10^{11}	160/280	[27]
NiO/n-Si	365	0	0.013	–	1.03×10^{11}	–	[28]
NiO/n-Si	365	−5	0.16	–	–	1500/700	[29]
NiO/n-Si	330	3	0.7	–	6.3×10^{13}	–	[30]
NiO/n-Si	365	5	1.73	–	–	–	[31]
NiO/Al_2O_3/n-Si	365	−5	15.8	5.4×10^3	1.14×10^{13}	0.08/0.184	This work

© 2024 The Author(s). Advanced Electronic Materials published by Wiley-VCH GmbH

2199160x, 2024, 9, Downloaded from https://onlinelibrary.wiley.com/doi/10.1002/aelm.202300909 by Test, Wiley Online Library on [27/11/2024]. See the Terms and Conditions (https://onlinelibrary.wiley.com/terms-and-conditions) on Wiley Online Library for rules of use; OA articles are governed by the applicable Creative Commons License

Acknowledgements

The authors acknowledge the financial support from National Key Research and Development Program of China (Grant No. 2019YFB2203404) and Yunnan Province Innovation Team Project (Grant No. 2018HC020).

Conflict of Interest

The authors declare no conflict of interest.

Data Availability Statement

The data that support the findings of this study are available from the corresponding author upon reasonable request.

Keywords

Al_2O_3 , heterojunction, NiO, UV photodetector

Received: December 29, 2023
Revised: May 16, 2024
Published online: July 15, 2024

[1] H. Chen, K. Liu, L. Hu, A. A. Al-Ghamdi, *X. Fang, Mater. Today.* **2015**, *18*, 493.
[2] E. Monroy, F. Omnès, F. Calle, *Semicond. Sci. Technol.* **2003**, *18*, R33.
[3] N. Nasiri, R. Bo, F. Wang, L. Fu, A. Tricoli, *Adv. Mater.* **2015**, *27*, 4336.
[4] G. Liu, M. Zhang, D. Zhang, X. Gu, F. Meng, S. Wen, Y. Chen, S. Ruan, *Appl. Surf. Sci.* **2014**, *315*, 55.
[5] K. Singh, N. Berwal, I. Rawal, S. Dahiya, R. Punia, R. Dhar, *J. Alloys Compd.* **2018**, *768*, 978.
[6] K. C. S. Reddy, P. Sahatiya, I. Santos-Sauceda, O. Cortázar, R. Ramírez-Bon, *Appl. Surf. Sci.* **2020**, *513*, 978.
[7] J. M. Choi, S. Im, *Appl. Surf. Sci.* **2005**, *244*, 435.
[8] S. Chaoudhary, A. Dewasi, V. Rastogi, R. N. Pereira, A. Sinopoli, B. Aïssa, A. Mitra, *Nanotechnology* **2022**, *33*, 255202.
[9] B. Parida, S. Kim, M. Oh, S. Jung, M. Baek, J. H. Ryou, H. Kim, *Mater. Sci. Semicond. Process.* **2017**, *71*, 29.
[10] G. Jayalakshmi, K. Saravanan, J. Navas, T. Arun, B. K. Panigrahi, *J Mater Sci Mater Electron* **2019**, *30*, 6811.
[11] D. Y. Jiang, X. Y. Zhang, Q. S. Liu, Z. H. Bai, L. P. Lu, X. C. Wang, D. Z. Shen, *Appl. Surf. Sci.* **2010**, *256*, 6153.
[12] C. Ling, T. Guo, W. Lu, Y. Xiong, L. Zhu, Q. Xue, *Nanoscale* **2017**, *9*, 8848.
[13] T. Wang, H. Wu, C. Chen, C. Liu, *Appl. Phys. Lett.* **2012**, 100.
[14] Y. Xu, H. Shen, B. Xu, Z. Wang, Y. Li, B. Lai, J. Zhang, *Nanotechnology* **2021**, *32*, 275502.
[15] H. Qian, X. Zhang, Y. Ma, L. Zhang, T. Chen, X. Wei, B. Zhang, *Vacuum* **2022**, *200*, 111019.
[16] T. C. Zhang, Y. Guo, Z. X. Mei, C. Z. Gu, X. L. Du, *Appl. Phys. Lett.* **2009**, 94.
[17] X. Liu, X. Deng, X. Li, H. C. Chiu, Y. Chen, V. D. Lin, C. H. Botcha, *J. Alloys Compd.* **2020**, *830*, 154716.
[18] R. V. Gonçalves, H. Wender, P. Migowski, A. F. Feil, D. Eberhardt, J. Boita, S. Khan, G. Machado, J. Dupont, S. R. Teixeira, *J. Phys. Chem. C* **2017**, *121*, 5855.
[19] J. Das, K. S. R. Menon, *Appl. Surf. Sci.* **2015**, *359*, 61.
[20] N. M. Terlinden, G. Dingemans, M. C. Van de Sanden, W. M. M. Kessels, *Appl. Phys. Lett.* **2010**, 96.
[21] H. Zou, X. Li, W. Peng, W. Wu, R. Yu, C. Wu, Z. L. Wang, *Adv. Mater.* **2017**, *29*, 1701412.
[22] X. Gong, M. Tong, Y. Xia, W. Cai, J. S. Moon, Y. Cao, A. J. Heeger, *Science* **2009**, *325*, 1665.
[23] X. Xu, J. Chen, S. Cai, Z. Long, Y. Zhang, L. Su, S. He, C. Tang, P. Liu, H. Peng, X. Fang, *Adv. Mater.* **2018**, *30*, 1803165.
[24] J. D. Hwang, M. C. Lin, *Sens. Actuators, A* **2023**, *349*, 114087.
[25] X. Xie, Z. Zhang, B. Li, S. Wang, D. Shen, *Opt. Express* **2015**, *23*, 32329.
[26] M. Jia, F. Wang, L. Tang, J. Xiang, K. S. Teng, S. P. Lau, Y. Lü, *Opt. Laser Technol.* **2023**, *157*, 108634.
[27] G. Shang, L. Tang, G. Wu, S. Yuan, M. Jia, X. Guo, K. S. Teng, *Sensors* **2023**, *23*, 2741.
[28] A. A. Ahmed, M. R. Hashim, T. F. Qahtan, M. Rashid, *Ceram. Int.* **2022**, *48*, 20078.
[29] N. H. Al-Hardan, N. M. Ahmed, M. A. Almessiere, A. A. Aziz, *Mater. Res. Express* **2020**, *6*, 126332.
[30] A. A. Hadi, B. A. Badr, R. O. Mahdi, K. S. Khashan, *Optik* **2020**, *219*, 165019.
[31] A. A. Ahmed, M. R. Hashim, T. F. Qahtan, M. Rashid, *Optik* **2022**, *255*, 168694.
[32] H. Chen, X. Ma, J. Zhang, Q. Li, H. Liu, Z. Chen, S. Chu, *Opt. Mater. Express* **2018**, *8*, 785.
[33] J. Yu, C. X. Shan, J. S. Liu, X. W. Zhang, B. H. Li, D. Z. Shen, *physica staus solidi (RRL)-Rapid Res. Lett.* **2013**, *7*, 425.

© 2024 The Author(s). Advanced Electronic Materials published by Wiley-VCH GmbH

2199160x, 2024, 9, Downloaded from https://onlinelibrary.wiley.com/doi/10.1002/aelm.202300909 by Test, Wiley Online Library on [27/11/2024]. See the Terms and Conditions (https://onlinelibrary.wiley.com/terms-and-conditions) on Wiley Online Library for rules of use; OA articles are governed by the applicable Creative Commons License